

# Photothermal direct methane conversion to formaldehyde at the gas-solid interface under ambient pressure

Received: 14 November 2024

Accepted: 5 March 2025

Published online: 15 March 2025

Yuxiong Wang<sup>1,4</sup>, Yaoyu Zhang<sup>2,4</sup>, Xiaoqiang Wang<sup>3</sup>, Yue Liu<sup>1</sup>✉ & Zhongbiao Wu<sup>1</sup>✉

Photocatalytic direct oxidation of methane to C<sub>1</sub> oxygenates offers a green alternative to conventional energy-intensive and high-carbon-footprint multi-step processes. However, current batch-type gas–liquid–solid reaction systems under high-pressure conditions face critical challenges in real-time product separation and concentration for industrial implementation. Here, we demonstrate a continuous-flow gas–solid photothermal catalytic route for methane conversion to formaldehyde under ambient pressure, where the generated gas-phase formaldehyde can be easily collected by water absorption. The Ag single-atom modified ZnO photocatalyst achieves a formaldehyde production rate of  $117.8 \pm 1.7 \mu\text{mol h}^{-1}$  with  $71.2 \pm 0.8\%$  selectivity. Meanwhile, a highly concentrated formaldehyde solution ( $514.2 \pm 33.7 \mu\text{mol mL}^{-1}$ ,  $1.54 \pm 0.10 \text{ wt.}\%$ ) is obtained through 12-hour water absorption, effectively overcoming the product enrichment barrier that plagues conventional batch reaction route. This study establishes a robust technological foundation for sustainable industrial-scale conversion of methane to value-added chemicals.

Direct conversion of methane (CH<sub>4</sub>) into value-added chemical products represents a cornerstone for advancing sustainable C<sub>1</sub> chemistry. Formaldehyde (HCHO), as a high-value CH<sub>4</sub> converting product, is widely used as a raw material for over 50 industrial processes<sup>1</sup>. Notably, HCHO is a promising hydrogen carrier, performing an important role in green energy. The hydrogenolysis of HCHO and water ( $\text{HCHO} + \text{H}_2\text{O} \rightarrow \text{HCOOH} + \text{H}_2$ ) meets the standards of “hydrogen economy”, and the theoretical hydrogen efficiency (8.4 wt.%) is higher than that of formic acid (4.4 wt.%)<sup>2</sup>. Additionally, oxygen effectively promotes the hydrogenolysis of HCHO and water on Ag/MgO, which can effectively solve the process of pre-eliminating molecular oxygen to avoid reverse hydrogen oxidation reactions<sup>3</sup>. However, current industrial HCHO production via methanol dehydrogenation at 500–600 °C remains plagued by multi-step complexity, excessive energy demands (40% methanol consumption), and substantial CO<sub>2</sub>

emissions<sup>4</sup>. This stark reality underscores the imperative for developing mild-condition one-step CH<sub>4</sub>-to-HCHO conversion systems to realize truly sustainable C<sub>1</sub> chemistry<sup>5</sup>.

Photocatalytic CH<sub>4</sub> oxidation to C<sub>1</sub> oxygenates (CH<sub>3</sub>OOH, CH<sub>3</sub>OH, HCHO, etc.) has become a research hotspot, enabling ambient-condition CH<sub>4</sub> activation using economical O<sub>2</sub> oxidants<sup>6–10</sup>. The current photocatalytic selective oxidation of CH<sub>4</sub> systems predominantly employ batch-type gas–liquid–solid reactors, which necessitate pressurized operation to enhance CH<sub>4</sub> solubility in aqueous media<sup>11–15</sup>. More critically, these systems suffer from progressive product degradation during batch cycling, thereby reducing the selectivity. To improve the selectivity, it is often solved by increasing the amount of water and continuous flow of water<sup>11,16</sup>, which will cause problems in subsequent purification and separation. If gas–solid photocatalytic selective oxidation of CH<sub>4</sub> is achieved under atmospheric pressure,

<sup>1</sup>Key Laboratory of Environment Remediation and Ecological Health, Ministry of Education, College of Environmental and Resource Sciences, Zhejiang University, Hangzhou, PR China. <sup>2</sup>School of Environment, Nanjing Normal University, Nanjing, PR China. <sup>3</sup>College of Biological, Chemical Science and Engineering, Jiaxing University, Jiaxing, PR China. <sup>4</sup>These authors contributed equally: Yuxiong Wang, Yaoyu Zhang. ✉e-mail: [yueliu@zju.edu.cn](mailto:yueliu@zju.edu.cn); [zbwu@zju.edu.cn](mailto:zbwu@zju.edu.cn)

similar to photocatalytic oxidative coupling of CH<sub>4</sub>, it is expected to resolve these limitations through continuous product desorption.

ZnO is widely utilized as a semiconductor catalyst for the photocatalytic conversion of CH<sub>4</sub> to HCHO<sup>14,17,18</sup>. Lattice oxygen can participate in the reactions to generate \*OCH<sub>3</sub> species and its further dehydrogenation to produce HCHO, and the consumed lattice oxygen is then replenished by dissociated O<sub>2</sub><sup>18</sup>. Therefore, manipulating the lattice oxygen mobility of metal oxides can effectively enhance the HCHO selectivity. While thermal activation can significantly enhance the activity of lattice oxygen, it can also lead to overoxidation of CH<sub>4</sub>. Single atoms (SAs) can regulate the microenvironment of the catalyst surface, effectively suppressing overoxidation of the target product<sup>19–21</sup>. Therefore, metal SAs-modified ZnO might be an ideal photocatalyst to achieve high HCHO yield and selectivity with the assistance of heat.

In this work, we rationally designed Ag SAs-modified ZnO (Ag<sub>i</sub>-ZnO) for gas–solid photothermal catalytic selective oxidation of CH<sub>4</sub> to HCHO in a flow reactor under atmospheric pressure. The Ag SAs accumulate photogenerated holes and activate H<sub>2</sub>O to generate \*OH species, which promote the C–H bond cleavage of CH<sub>4</sub>. In addition, Ag SAs alter the local electron distribution of ZnO, which is beneficial for the generation and desorption of \*HCHO to generate gas-phase HCHO. Furthermore, the assistance of heat promotes the separation of photogenerated electrons and holes, and enhances the mobility of surface lattice oxygen, thus promoting the formation of HCHO. As a result, Ag<sub>i</sub>-ZnO catalyst demonstrates a HCHO production rate of 117.8 ± 1.7 μmol h<sup>−1</sup> with 71.2 ± 0.8% selectivity. After 12 h of aqueous-phase absorption of the reaction effluents, the HCHO concentration reaches 514.2 ± 33.7 μmol mL<sup>−1</sup> (1.54 ± 0.10 wt.%). The absorption trapping process also provides a co-benefit that the cogenerated CH<sub>3</sub>OH (28.1 ± 1.1 μmol mL<sup>−1</sup>) in the solution can effectively inhibit the polymerization of HCHO. This work establishes an environmentally benign and energy-efficient strategy for the practical industrial application of direct CH<sub>4</sub> to HCHO under mild operating conditions.

## Results

### Catalyst screening and characterizations

To screen metallic SAs-modified ZnO (M<sub>i</sub>-ZnO) catalysts for the gas–solid photothermal catalytic selective oxidation of CH<sub>4</sub> to HCHO, density functional theory (DFT) calculations were performed. The key step in the photothermal catalytic selective oxidation of CH<sub>4</sub> to HCHO is the effective desorption of HCHO from the catalyst to prevent its excessive oxidation<sup>11,22,23</sup>. Therefore, the ZnO (101) model is selected for modeling HCHO adsorption on metallic SAs modified catalysts. As shown in Fig. 1a, the adsorption energy of HCHO (*E*<sub>ads</sub>) on M<sub>i</sub>-ZnO follows the order: Ag<sub>i</sub>-ZnO (−1.10 eV) < Au<sub>i</sub>-ZnO (−1.41 eV) < Pt<sub>i</sub>-ZnO (−1.51 eV) < Pd<sub>i</sub>-ZnO (−1.56 eV), indicating Ag SAs incorporation can effectively promote HCHO generation. Based on theoretical simulation results, a series of metal SAs (Ag, Au, Pt, and Pd) modified ZnO (Supplementary Fig. 1) were synthesized for photothermal catalytic oxidation of CH<sub>4</sub>. It is found that Ag<sub>i</sub>-ZnO with the lowest HCHO adsorption energy shows the highest HCHO generation rate and selectivity (Fig. 1b). There is a good correlation between HCHO/(CO + CO<sub>2</sub>) in the photothermal catalytic oxidation of CH<sub>4</sub> on M<sub>i</sub>-ZnO and the adsorption energy of HCHO on M<sub>i</sub>-ZnO in DFT calculations (Fig. 1c), indicating that metal SAs doping can effectively regulate the adsorption performance of HCHO to control the photothermal catalytic selective oxidation of CH<sub>4</sub> to HCHO. Based on theoretical and experimental results, a specific study is then conducted on the photothermal catalytic selective oxidation of CH<sub>4</sub> to HCHO on Ag<sub>i</sub>-ZnO samples in reference to pure ZnO and Ag nanoparticle-modified ZnO (Ag<sub>NP</sub>-ZnO).

The fabricated ZnO exhibits nanoparticles with an average size of approximately 22.7 nm (Supplementary Fig. 2a, b). The high-resolution

transmission electron microscopy (HRTEM) image (Supplementary Fig. 2c) shows the lattice fringes of ZnO with an interplanar spacing of 0.247 nm, corresponding to the (101) plane of ZnO. The Ag<sub>i</sub>-ZnO and Ag<sub>NP</sub>-ZnO samples were obtained through a simple 85 °C bath assisted NaH<sub>2</sub>PO<sub>2</sub> reduction method by regulating the amounts of AgNO<sub>3</sub> and NaH<sub>2</sub>PO<sub>2</sub>. The actual loading amounts of Ag in Ag<sub>i</sub>-ZnO and Ag<sub>NP</sub>-ZnO are 0.18 wt.% and 0.96 wt.%, respectively, as measured by inductively coupled plasma–optical emission spectroscopy (ICP–OES). The X-ray diffraction (XRD) spectra of all prepared samples (Supplementary Fig. 3) are well indexed to the typical hexagonal wurtzite structure of ZnO (JCPDS file no. 36-1451)<sup>24</sup>. No characteristic diffraction peaks of Ag can be observed on either Ag<sub>i</sub>-ZnO or Ag<sub>NP</sub>-ZnO, demonstrating the small size and good dispersion of Ag species on ZnO. For Ag<sub>i</sub>-ZnO, the Ag species remain highly dispersed on the ZnO NPs from the energy-dispersive X-ray spectroscopy (EDS) elemental mapping images (Fig. 2a). The Ag atoms can be observed from the aberration-corrected high-angle annular dark-field scanning TEM (AC-HAADF-STEM) image due to its being much brighter than Zn atoms (Fig. 2b). Furthermore, a lattice spacing of 0.236 nm corresponding to the Ag (111) plane appears in the Ag<sub>NP</sub>-ZnO sample (Supplementary Fig. 4a), and the EDS elemental mapping image (Supplementary Fig. 4b) further verifies the formation of Ag NPs in the Ag<sub>NP</sub>-ZnO sample. And the average size of Ag NPs on Ag<sub>NP</sub>-ZnO sample is around 12.9 nm (Supplementary Fig. 4c, d). Moreover, the ultraviolet–visible diffuse reflectance spectroscopy (UV–Vis DRS) (Supplementary Fig. 5) clearly shows that only the Ag<sub>NP</sub>-ZnO sample exhibits a surface plasmon peak, which also proves the formation of Ag NPs and Ag SAs in Ag<sub>NP</sub>-ZnO and Ag<sub>i</sub>-ZnO samples, respectively.

To further explore the local structure of Ag species in Ag<sub>i</sub>-ZnO and Ag<sub>NP</sub>-ZnO, X-ray photoelectron spectroscopy (XPS) and synchrotron X-ray absorption spectroscopy (XAS) were carried out. The X-ray absorption near-edge structure (XANES) spectrum at the Ag K-edge of Ag<sub>NP</sub>-ZnO (Fig. 2c) shows a similar white-line intensity to that of the Ag foil, indicating that metallic Ag is the dominant Ag species in Ag<sub>NP</sub>-ZnO. The white line for Ag<sub>i</sub>-ZnO is between Ag foil and Ag<sub>2</sub>O, indicating that the strong metal–support interaction leads to the formation of partially oxidized Ag species (Ag<sup>0</sup> < Ag<sup>δ+</sup> < Ag<sup>+</sup>) (Fig. 2c). The states of Ag species of Ag<sub>i</sub>-ZnO and Ag<sub>NP</sub>-ZnO are also confirmed by the XPS results (Supplementary Fig. 6). The Fourier-transformed k<sup>3</sup> weighted extended X-ray absorption fine structure (EXAFS) spectra at the Ag K-edge of Ag<sub>i</sub>-ZnO (Fig. 2d) display a prominent Ag–O shell peak at 1.59 Å, and there is no Ag–Ag shell, confirming the atomic dispersion of Ag in Ag<sub>i</sub>-ZnO. The Ag<sub>NP</sub>-ZnO sample shows a major peak at the Ag–Ag shell, indicating that Ag species appear as metallic NPs. Wavelet transform EXAFS analysis (Fig. 2e) further visualizes structural information. Furthermore, EXAFS fitting analysis was conducted to determine the coordination configurations of Ag<sub>i</sub>-ZnO. According to the best-fitted EXAFS (Supplementary Fig. 7, and Supplementary Table 1), the coordination number of Ag–O (2.06 Å) is estimated to be 2 for Ag<sub>i</sub>-ZnO. Then, DFT calculations were carried out to acquire the structure of Ag<sub>i</sub>-ZnO. In Ag<sub>i</sub>-ZnO, each Ag atom binds to two O atoms (Supplementary Fig. 7c), which is consistent with the EXAFS fitting result.

### Photothermal catalytic selective oxidation of CH<sub>4</sub> to HCHO

Photothermal catalytic oxidation of CH<sub>4</sub> was investigated in a 50-mL gas–solid flow reactor with irradiation of a 300-W Xe lamp (λ = 200–1200 nm, 1000 mW cm<sup>−2</sup>) under external heating at 150 °C (Supplementary Fig. 8). The obtained HCHO reaches stability after 60 min of illumination (Supplementary Fig. 11 and Supplementary Table 3). For comparison, the products of each sample are analyzed after 180 min of light exposure. A mixture of 50 mL min<sup>−1</sup> CH<sub>4</sub>/air (25 vol.% O<sub>2</sub>/N<sub>2</sub>) = 45:5 and 20% relative humidity (RH) was used as the feed gas after screening under preliminary conditions (Supplementary Fig. 12 and Supplementary Tables 4–7). As shown in Fig. 3a and Supplementary Table 8, the yield of HCHO over Ag<sub>i</sub>-ZnO sample is

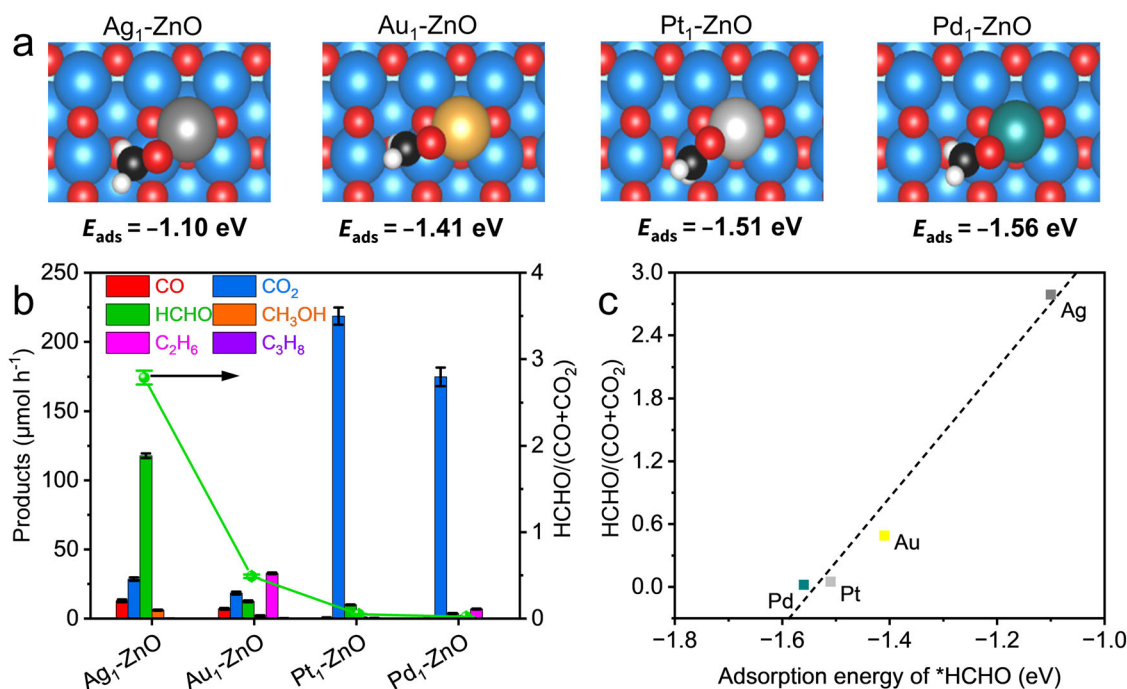


**Fig. 1 | Screening of M<sub>1</sub>-ZnO for photothermal catalytic selective oxidation of CH<sub>4</sub> to HCHO. a** Calculated adsorption energy of HCHO ( $E_{\text{ads}}$ ) on M<sub>1</sub>-ZnO. **b** Gas-solid photothermal catalytic CH<sub>4</sub> oxidation performance for M<sub>1</sub>-ZnO. **c** HCHO/(CO + CO<sub>2</sub>) of gas-solid photothermal catalytic CH<sub>4</sub> oxidation for M<sub>1</sub>-ZnO plotted against the HCHO adsorption on M<sub>1</sub>-ZnO. The reaction conditions in (b): CH<sub>4</sub>

(45 mL min<sup>-1</sup>) + air (5 mL min<sup>-1</sup>), RH = 20%, external heating at 150 °C, Xe lamp with wavelength range of 200–1200 nm and 1000 mW cm<sup>-2</sup> light intensity. Blue, red, black, white, dark gray, yellow, light gray and turquoise spheres in (a) represent Zn, O, C, H, Ag, Au, Pt and Pd atoms, respectively. Source data are provided as a Source Data file.

117.8 ± 1.7 μmol h<sup>-1</sup>, which is approximately 2.2 times higher than that over pure ZnO. The introduction of Ag SAs increases the HCHO selectivity from 59.6 ± 0.9% to 71.2 ± 0.8%. And the valuable products (CO, CH<sub>3</sub>OH and HCHO) generated over Ag<sub>1</sub>-ZnO sample reach 136.8 ± 3.1 μmol h<sup>-1</sup> with a selectivity of 82.7 ± 0.3%, and the CH<sub>4</sub> conversion on Ag<sub>1</sub>-ZnO is 0.14 ± 0.003%. When the surface temperature of the catalyst is controlled at 228 °C, the apparent quantum yield (AQY) values of HCHO at 365, 400 and 420 nm on Ag<sub>1</sub>-ZnO are 20.19 ± 2.32%, 1.98 ± 0.31% and 0.05 ± 0.01%, respectively (Supplementary Fig. 13). The activity of ZnO sample treated with NaH<sub>2</sub>PO<sub>2</sub> (ZnO(SM)) is basically consistent with that of pure ZnO, indicating that simple NaH<sub>2</sub>PO<sub>2</sub> treatment has no effect on the activity of ZnO. Notably, the HCHO production rate of Ag<sub>1</sub>-ZnO can reach 11.8 ± 0.4 μmol h<sup>-1</sup> with a selectivity of 72.1 ± 1.3% under simulated sunlight (AM 1.5 G, 100 mW cm<sup>-2</sup>) when the surface temperature of catalyst is the same as the above temperature (Supplementary Fig. 14 and Supplementary Table 9). However, a bare HCHO yield (8.1 ± 0.5 μmol h<sup>-1</sup>) and a large amount of produced CO<sub>2</sub> (80.0 ± 1.6 μmol h<sup>-1</sup>) over Ag<sub>NP</sub>-ZnO sample are achieved, indicating that the presence of Ag NPs leads to the over-oxidation of CH<sub>4</sub>. The HCHO yield obtained from the gas-solid photothermal catalytic oxidation of CH<sub>4</sub> over Ag<sub>1</sub>-ZnO under atmospheric pressure is not only higher than all reported photocatalytic systems (Supplementary Table 14)<sup>11–15,17,18,22,23,25,26</sup>, but also still possesses superiority compare to traditional high-pressure and high-temperature catalytic reaction systems (Supplementary Table 15)<sup>27–35</sup>.

The yield and selectivity of HCHO increase with the increasing of external heating temperature (<150 °C) under 1000 mW cm<sup>-2</sup> light intensity irradiation, and the activity cannot be further increased at a higher temperature (Fig. 3b and Supplementary Table 10). The surface temperature of Ag<sub>1</sub>-ZnO sample reaches approximately 228 °C under external heating at 150 °C during the reaction (Supplementary Fig. 15). The HCHO yield is almost directly proportional to the light intensity on Ag<sub>1</sub>-ZnO when the surface temperature of the catalyst is controlled at

228 °C by heating (Fig. 3c and Supplementary Table 11). Only CO and CO<sub>2</sub> are generated on 250 °C on Ag<sub>1</sub>-ZnO in the absence of light (Supplementary Fig. 14). These results fully demonstrate that the HCHO production is driven by light rather than heat. Heat input may promote the separation of photo-generated charge carriers and HCHO desorption, thereby promoting the generation of gas-phase HCHO. The results of comparative experiments demonstrate that no products are detected without photocatalysts or CH<sub>4</sub> feed (Supplementary Fig. 14 and Supplementary Table 9), indicating that all products are derived from photothermal catalytic oxidation of CH<sub>4</sub>. Bare HCHO are obtained over Ag<sub>1</sub>-ZnO under visible (Vis)-light (λ > 420 nm) (Supplementary Fig. 14), indicating that the HCHO is mainly generated by UV excitation.

A long-term test was carried out to assess the stability of the Ag<sub>1</sub>-ZnO sample. The HCHO yield gradually decreases to 92.1 μmol h<sup>-1</sup> after a long-term test of 12 h, and the activity of the catalyst reacted for 12 h can be restored after ultrasonic washing with ultrapure water (Fig. 3d and Supplementary Table 12). The HAADF-STEM image and the corresponding EDS elemental mapping, the magnified high-resolution AC-HAADF-STEM image, and XAFS of spent Ag<sub>1</sub>-ZnO (Supplementary Fig. 16) shows that Ag SAs are well retained after the long-term test. The XRD result confirms the stable crystalline structure of Ag<sub>1</sub>-ZnO after the long-term test (Supplementary Fig. 17). The XPS result of the spent Ag<sub>1</sub>-ZnO (Supplementary Fig. 18) indicates the consumption of lattice oxygen and surface carbon deposition after the long-term test. Additionally, the O<sub>2</sub>-TPO results show significant CO<sub>2</sub> generation over the spent Ag<sub>1</sub>-ZnO when the temperature rises to around 130 °C (Supplementary Fig. 19). The above results indicate that the activity attenuation of Ag<sub>1</sub>-ZnO is mainly caused by carbon deposition and the inability of lattice oxygen regeneration in a timely manner.

To elucidate the advantages of gas-solid photothermal catalytic selective oxidation of CH<sub>4</sub> to HCHO in a flow reactor, the gas after reaction over Ag<sub>1</sub>-ZnO was absorbed for 3, 6 and 12 h with 2 mL of



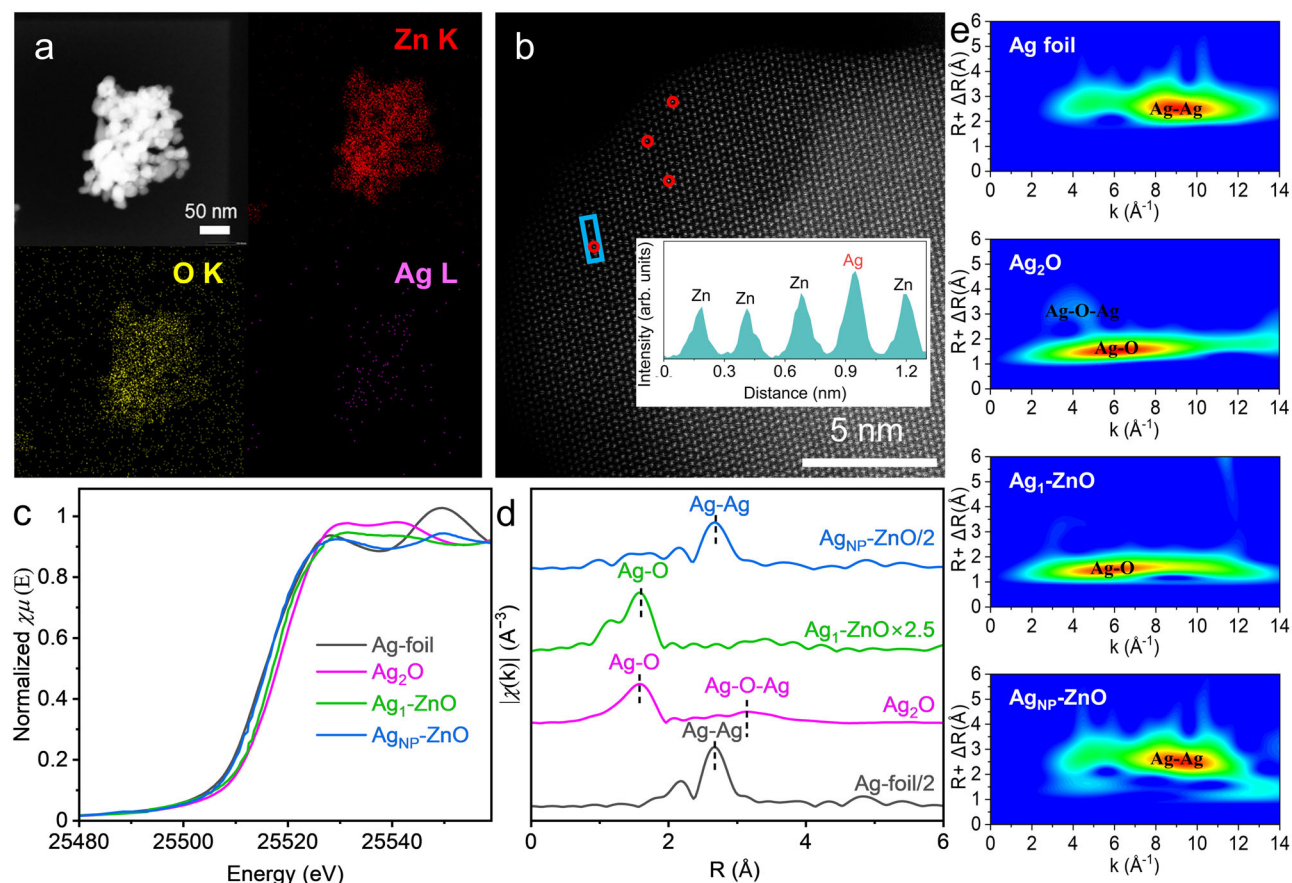


**Fig. 2 | Catalyst characterizations.** **a** HAADF-STEM image and the corresponding EDS elemental mapping signals of Ag<sub>1</sub>-ZnO. **b** Magnified high-resolution AC-HAADF-STEM image of Ag<sub>1</sub>-ZnO and the corresponding intensity profile from the marked position. **c** The normalized XANES spectra at the Ag K-edge. **d** The k<sup>3</sup>-

weighted Fourier transform EXAFS spectra at the Ag K-edge. **e** Wavelet transformation for the k<sup>3</sup>-weighted EXAFS signal at the Ag K-edge. Source data are provided as a Source Data file.

distilled water at 0 °C. The HCHO concentrations in the absorption solution at 3, 6 and 12 h are determined to be  $160.9 \pm 5.4$ ,  $297.1 \pm 15.8$  and  $514.2 \pm 33.7 \mu\text{mol mL}^{-1}$ , respectively (Fig. 3e, Supplementary Fig. 20 and Supplementary Table 13). At the same time, there is a small amount of CH<sub>3</sub>OH in the absorption solution, which can effectively prevent the polymerization of HCHO. The  $514.2 \pm 33.7 \mu\text{mol mL}^{-1}$  ( $1.54 \pm 0.10$  wt.%) of HCHO solution obtained from the gas–solid atmospheric pressure photothermal catalytic reaction over Ag<sub>1</sub>-ZnO outperforms all state-of-the-art photocatalysts (Fig. 3f and Supplementary Table 14)<sup>11–15,17,18,22,23,25</sup>, whether it is a gas–liquid–solid batch reaction or continuous flow reaction. It can be observed that this strategy can effectively solve the problems of products not being separated or concentrated in a timely manner in gas–liquid–solid reactions<sup>13,22</sup>. In addition, after 12-hour absorption of the gases from reactor, the absorption rates of HCHO and CH<sub>3</sub>OH can still reach  $81.2 \pm 5.1\%$  and  $91.1 \pm 3.6\%$ , respectively, indicating that it can be expected to synthesize industrial grade HCHO solutions with the extension of reaction time and the expansion of reactor scale. In summary, the gas–solid photothermal catalysis method for CH<sub>4</sub> direct conversion to HCHO is of good industrial application prospects.

### Insight into mechanism

To explore the origin of the high HCHO activity and selectivity over Ag<sub>1</sub>-ZnO, the charge separation efficiency of the catalysts was studied by photocurrent and electrochemical impedance measurements. ZnO has the lowest photocurrent density ( $22.5 \mu\text{A cm}^{-2}$ ), which is increased by approximately 2.3 and 2.9 times for Ag<sub>1</sub>-ZnO and Ag<sub>NP</sub>-ZnO,

respectively (Supplementary Fig. 21a). The electrochemical impedance results (Supplementary Fig. 21b) show that the electron transmission resistance decreases in the order of ZnO > Ag<sub>1</sub>-ZnO > Ag<sub>NP</sub>-ZnO. Furthermore, in situ steady-state photoluminescence (PL) was carried out to explore the thermal assistant effect. The PL peak is significantly quenched with increasing temperature in all samples, indicating that heat can improve the internal charge separation of photocatalysts (Supplementary Fig. 22). The weaker PL peaks for Ag<sub>1</sub>-ZnO and Ag<sub>NP</sub>-ZnO exhibit significantly suppressed charge recombination rates at both 25 and 250 °C (Supplementary Fig. 23), which is in good agreement with the photocurrent and electrochemical impedance analysis. The above results demonstrate that the introduction of Ag species and the heat input greatly improve the charge separation efficiency, which is conducive to the yield of oxygenates in photothermal catalytic CH<sub>4</sub> oxidation.

In situ electron spin resonance (in situ ESR) was carried out to understand the charge transport behavior in the presence of H<sub>2</sub>O and O<sub>2</sub> on all samples. The signal at  $g = 2.000$  belonging to oxygen vacancies is only observed on Ag<sub>NP</sub>-ZnO (Fig. 4a)<sup>36,37</sup>, indicating that Ag NPs contribute to the formation of oxygen vacancies on ZnO. Under illumination, the ESR signal at  $g = 1.959$  (Zn<sup>•+</sup>) in all samples increases rapidly<sup>37</sup>. The order of peak intensity is: Ag<sub>1</sub>-ZnO > Ag<sub>NP</sub>-ZnO > ZnO (Fig. 4a), which is inconsistent with the photoelectrochemical results. It may be due to the fact that Ag SAs as a hole acceptor promote the transfer of electrons to Zn<sup>2+</sup>, while Ag NPs as an electron acceptor reduce the amount of Zn<sup>•+</sup>. To confirm this speculation, in situ near-ambient pressure X-ray photoelectron spectroscopy (in situ NAP-XPS) was then performed. For the Ag<sub>1</sub>-ZnO sample, Zn 2p peaks exhibit a

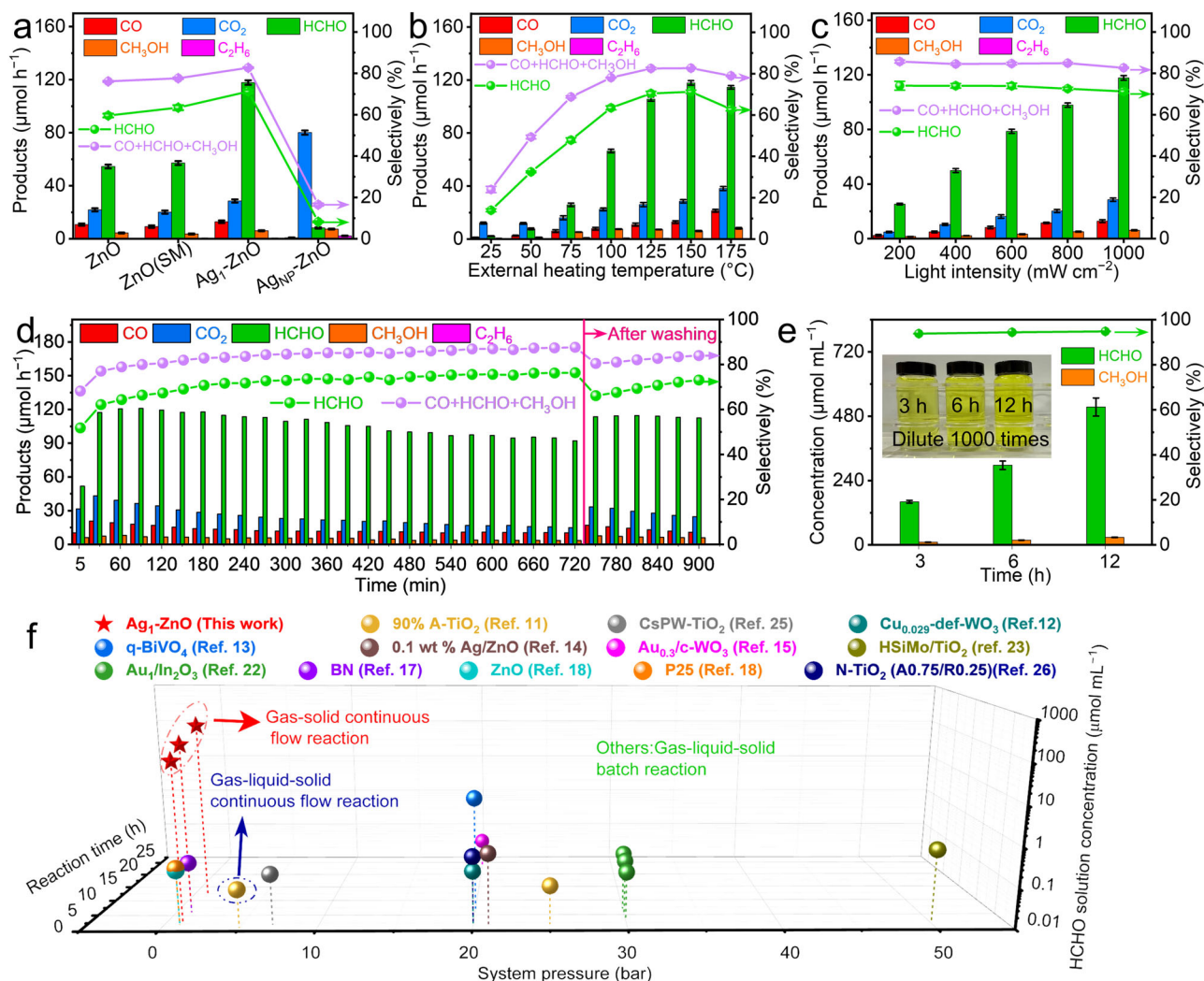


**Fig. 3 | Activity of photothermal catalytic selective oxidation of CH<sub>4</sub> to HCHO.**

**a** Activity on ZnO, ZnO(SM), Ag<sub>1</sub>-ZnO, and Ag<sub>NP</sub>-ZnO under external heating at 150 °C. **b** Activity on Ag<sub>1</sub>-ZnO under external heating at different temperatures. **c** Activity on Ag<sub>1</sub>-ZnO at a catalyst surface temperature of 228 °C under irradiation with different light intensities. **d** Continuous stability tests on Ag<sub>1</sub>-ZnO. **e** Concentration of the absorption solution (2 mL distilled water at 0 °C) for a 3, 6

and 12 h of reaction. (The insert is a photo of the chromogenic agent added to the absorption solution after dilution 1000 times). **f** Comparison of the catalytic activity for photooxidation of CH<sub>4</sub> to HCHO over Ag<sub>1</sub>-ZnO with other photocatalysts. The reaction conditions in **a–d**: CH<sub>4</sub> (45 mL min<sup>-1</sup>) + air (5 mL min<sup>-1</sup>), and RH = 20%. Source data are provided as a Source Data file.

negative shift (Fig. 4c), indicating that Zn<sup>2+</sup> works as the electron acceptor under irradiation. And the Ag 3d peaks also show a negative binding energy shift (Fig. 4d), indicating the increase in valence state of Ag, which is different from most of other elements<sup>38,39</sup>. The peak at 531.7 eV (Supplementary Fig. 25) attributed to the oxygen species near oxygen vacancies does not change much<sup>40</sup>. These results show direct evidence that Ag SAs act as the hole acceptor during photocatalytic reaction. For Ag<sub>NP</sub>-ZnO sample, the signals for Ag 3d and Zn 2p separately exhibit a positive and a small negative shift (Supplementary Fig. 26a, c), and the peak at 531.7 eV is enhanced (Supplementary Fig. 26b), which support that the electrons on Zn<sup>+</sup> can transfer to the Ag NPs and the holes transfer to the lattice oxygen for activation. Meanwhile, as temperature rising, the peak intensity of Zn<sup>+</sup> increases on all samples (Fig. 4b and Supplementary Fig. 24a, b), indicating that heat input facilitates the separation of photogenerated electrons and holes. Compared with those obtained under Ar flow, the peak of Zn<sup>+</sup> drops and the peak of oxygen vacancies disappears after O<sub>2</sub> addition on Ag<sub>1</sub>-ZnO under illumination (Supplementary Fig. 24c), which is mainly due to O<sub>2</sub> consuming the electrons of Zn<sup>+</sup> and the activated O<sub>2</sub> can fill oxygen vacancies. The intensity of Zn<sup>+</sup> in the presence of H<sub>2</sub>O

significantly increase compared with that obtained under Ar or O<sub>2</sub> flow. The holes on Ag atoms are effectively consumed by H<sub>2</sub>O, promoting the separation of photo-generated electrons and hole, and thus achieving a large amount of Zn<sup>+</sup> generation.

To verify the effect of Ag species on the gas–solid photothermal catalytic oxidation of CH<sub>4</sub>, the intermediate steps were dynamically monitored on different samples by in situ diffuse reflectance infrared Fourier transform spectroscopy (in situ DRIFTS). For ZnO and Ag<sub>1</sub>-ZnO, the same characteristic peaks are observed. Upon light irradiation, the vibrational modes of \*CH<sub>3</sub> deformation (1156 cm<sup>-1</sup>)<sup>41</sup>, and the stretching vibrations of the C–H bond (2861 cm<sup>-1</sup>) and C–O bond (1075 cm<sup>-1</sup>) in the absorbed \*OCH<sub>3</sub> species appear immediately (Fig. 4e and Supplementary Fig. 27)<sup>42–44</sup>, indicating that CH<sub>4</sub> is rapidly dissociated into \*CH<sub>3</sub> and exists in the form of \*OCH<sub>3</sub> over ZnO and Ag<sub>1</sub>-ZnO. Furthermore, the peaks of \*CH<sub>2</sub> stretching (1430 cm<sup>-1</sup>) and \*HCHO species (2720 cm<sup>-1</sup>) gradually increase with the prolonged light irradiation<sup>45,46</sup>. Since the formation of HCHO via the conversion of CH<sub>3</sub>OH has been excluded (Supplementary Fig. 28), the results presented above suggest that the target product (HCHO) is generated from the conversion of the \*CH<sub>2</sub> intermediate, which comes from the

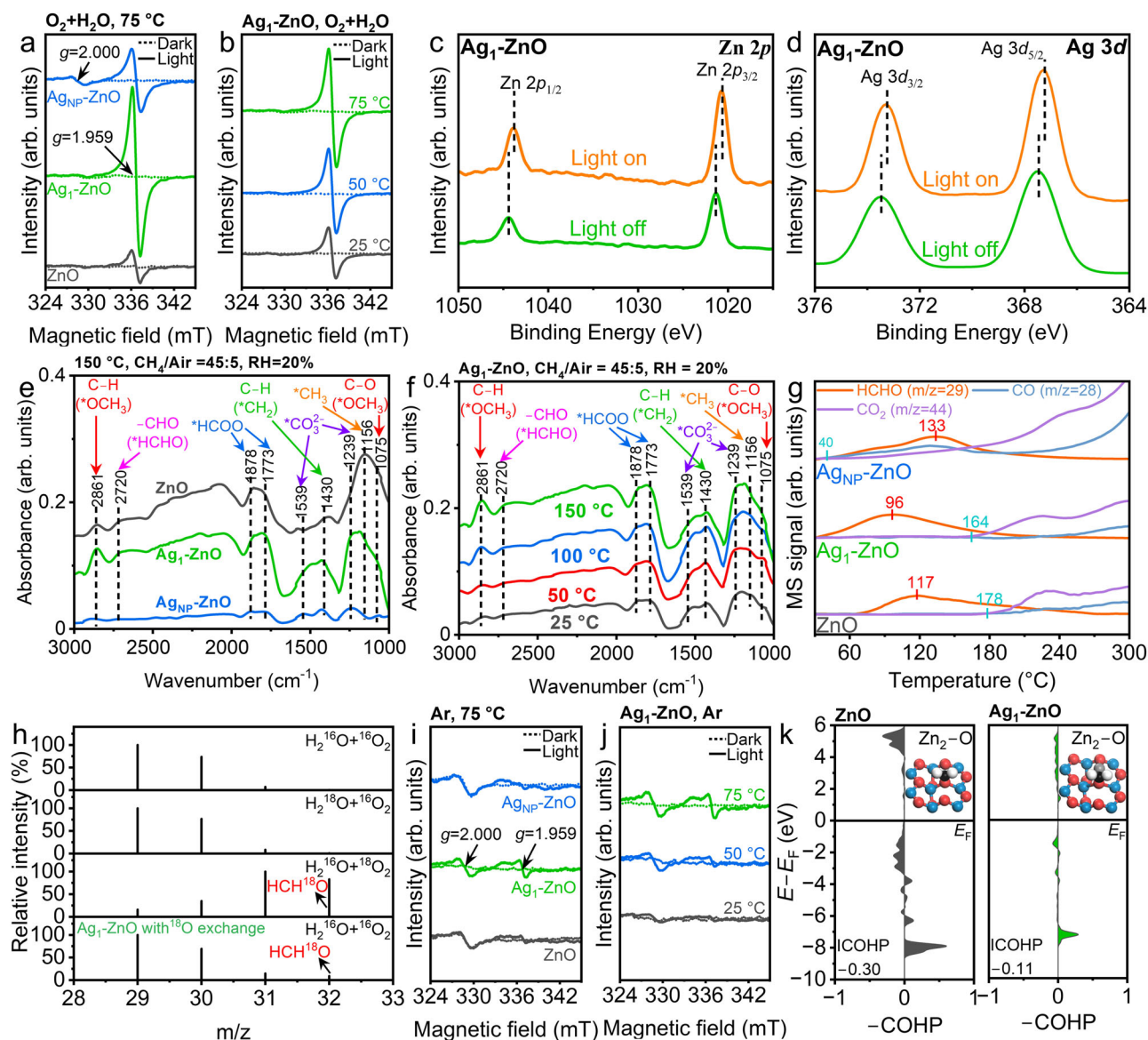


**Fig. 4 | Mechanistic studies.** In situ ESR spectra of different samples at 75 °C (a), and  $\text{Ag}_1\text{-ZnO}$  at different temperatures (b) in  $\text{O}_2 + \text{H}_2\text{O}$  in the dark (dashed line) and after 10 min of light irradiation (solid line). In situ NAP-XPS of Zn 2p (c) and Ag 3d (d) over  $\text{Ag}_1\text{-ZnO}$  under dark and light irradiation. In situ DRIFTS of photothermal catalytic oxidation of  $\text{CH}_4$  over different samples under external heating at 150 °C (e) and over  $\text{Ag}_1\text{-ZnO}$  under different external heating temperatures (f). g HCHO-TPD spectra of different samples. h GC-MS of HCHO produced by photothermal catalytic oxidation of  $\text{CH}_4$  with  $\text{H}_2^{16}\text{O} + ^{16}\text{O}_2$ ,  $\text{H}_2^{16}\text{O} + ^{18}\text{O}_2$  or  $\text{H}_2^{18}\text{O} + ^{16}\text{O}_2$  over  $\text{Ag}_1\text{-ZnO}$ .

$\text{ZnO}$  or  $\text{Ag}_1\text{-ZnO}$  with  $^{18}\text{O}$  exchange. In situ ESR spectra of different samples in Ar at 75 °C (i), and  $\text{Ag}_1\text{-ZnO}$  in Ar at different temperatures (j) in the dark (dashed line) and after 10 min of light irradiation (solid line). k COHP and ICOHP for adsorption of  $^*\text{CH}_2$  intermediates on the lattice oxygen over  $\text{ZnO}$  and  $\text{Ag}_1\text{-ZnO}$  slabs. The reaction conditions in (a), (b), (d):  $\text{CH}_4$  (45 mL min $^{-1}$ ) + air (5 mL min $^{-1}$ ), and RH = 20%. Blue, red, black, white, and dark gray spheres in (k) represent Zn, O, C, H and Ag atoms, respectively. Source data are provided as a Source Data file.

further dehydrogenation of  $^*\text{CH}_3$ . Meanwhile, the growth of  $^*\text{HCOO}$  (1878 and 1773  $\text{cm}^{-1}$ ) and  $^*\text{CO}_3^{2-}$  (1539 and 1239  $\text{cm}^{-1}$ ) species is assigned to the overoxidation of  $\text{CH}_4$ <sup>47–49</sup>. All peaks show stronger intensity on  $\text{Ag}_1\text{-ZnO}$ , indicating that the doping of Ag SAs is beneficial for the dehydrogenation of  $\text{CH}_4$  to HCHO. In contrast, intense  $^*\text{HCOO}$  and  $^*\text{CO}_3^{2-}$  species and weak  $^*\text{OCH}_3$  and  $^*\text{HCHO}$  intermediates can be observed for  $\text{Ag}_{\text{NP}}\text{-ZnO}$  (Fig. 4e, Supplementary Fig. 27), demonstrating that  $\text{CH}_4$  is more prone to overoxidation with the loading of Ag NPs. As the temperature increases, a significant increase in  $^*\text{OCH}_3$  and  $^*\text{HCHO}$  species can be observed over  $\text{Ag}_1\text{-ZnO}$ , accompanied by the raise in the likelihood of excessive oxidation (Fig. 4f). Therefore, the selection of an appropriate reaction temperature can effectively promote the selective oxidation of  $\text{CH}_4$  to HCHO. In addition, the HCHO-TPD experiment was used to investigate the oxidation and desorption

of HCHO on various catalysts. It can be seen that the desorption peak of HCHO located at 96 °C over  $\text{Ag}_1\text{-ZnO}$  is much lower than that of  $\text{ZnO}$  (117 °C) and  $\text{Ag}_{\text{NP}}\text{-ZnO}$  (178 °C), indicating its easier HCHO desorption feature. HCHO begins to decompose into CO at approximately 40 °C and  $\text{CO}_2$  is released as the temperature increases over  $\text{Ag}_{\text{NP}}\text{-ZnO}$ , demonstrating that the loading of Ag NPs effectively promotes the decomposition of HCHO and the activation of lattice oxygen. Hence, the loading of Ag SAs on  $\text{ZnO}$  facilitates the formation and desorption of  $^*\text{HCHO}$ ; while the loading of Ag NPs on  $\text{ZnO}$  promotes  $^*\text{HCHO}$  adsorption and activation of oxygen, leading to lower HCHO selectivity and the overoxidation of  $\text{CH}_4$ .

To obtain an in-depth understanding of gas–solid photo-thermal catalytic selective oxidation of  $\text{CH}_4$  to HCHO over  $\text{Ag}_1\text{-ZnO}$ , a series of isotope labeling experiments were carried out.



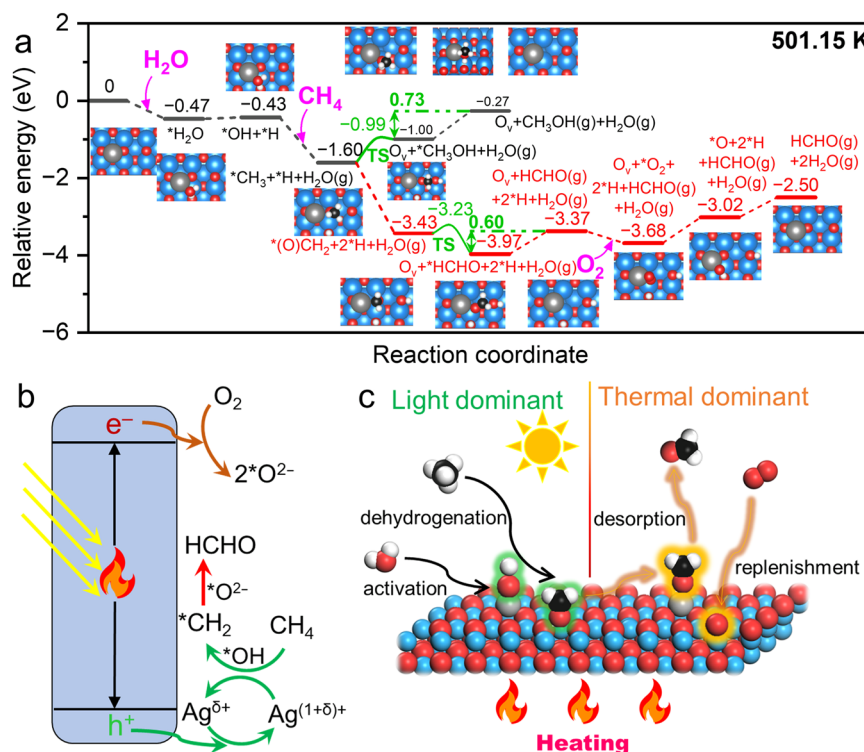


**Fig. 5 | DFT calculations and the proposed reaction mechanism.** **a** Calculated Gibbs free energy diagrams for CH<sub>4</sub> oxidation to HCHO or CH<sub>3</sub>OH at 501.15 K on Ag<sub>1</sub>-ZnO. Proposed reaction mechanism for gas–solid photothermal catalytic selective oxidation of CH<sub>4</sub> to HCHO on Ag<sub>1</sub>-ZnO from the energy band structure (**b**)

and the molecular level (**c**). The inset images in (**a**) are the optimized configurations of the corresponding reaction intermediates. Blue, red, black, white and dark gray spheres in (**a**) and (**c**) represent Zn, O, C, H and Ag atoms, respectively. Source data are provided as a Source Data file.

The C–H bond fracture process of CH<sub>4</sub> is elucidated in the reaction with <sup>18</sup>O<sub>2</sub> and D<sub>2</sub><sup>16</sup>O. As displayed in Supplementary Fig. 29, the generated water mainly exists in the form of HD<sup>16</sup>O, implying that hydrolyzed hydroxyl species mainly contribute to the dissociation of the C–H bond in CH<sub>4</sub>. The source of oxygen in the products during the reaction was also determined through isotope labeling experiments. All signals in CH<sub>3</sub>OH and HCHO remain basically unchanged with <sup>16</sup>O<sub>2</sub> and H<sub>2</sub><sup>18</sup>O (Supplementary Fig. 30a, c), while HCH<sup>18</sup>O and CH<sub>3</sub><sup>18</sup>OH are observed in the reaction with <sup>18</sup>O<sub>2</sub> and H<sub>2</sub><sup>16</sup>O (Supplementary Fig. 30e), indicating that O<sub>2</sub> is the oxygen source for HCHO and CH<sub>3</sub>OH. The generated CO<sub>2</sub> is mainly in the form of C<sup>16</sup>O<sup>18</sup>O with H<sub>2</sub><sup>18</sup>O and <sup>16</sup>O<sub>2</sub> or H<sub>2</sub><sup>16</sup>O<sub>2</sub> and <sup>18</sup>O<sub>2</sub> (Supplementary Fig. 30b, d, f), demonstrating that H<sub>2</sub>O is involved in the overoxidation of HCHO and CH<sub>3</sub>OH. To clearly demonstrate that lattice oxygen can participate in the reaction, the reaction over Ag<sub>1</sub>-ZnO after <sup>18</sup>O exchange was performed<sup>44,48</sup>. CH<sub>3</sub><sup>18</sup>OH and C<sup>16</sup>O<sup>18</sup>O are monitored over Ag<sub>1</sub>-ZnO after <sup>18</sup>O exchange, confirming that the surface lattice O in the ZnO participates in the oxidation of CH<sub>4</sub> (Supplementary Fig. 31). In addition, the GC-MS results of HCHO product in isotope experiments (Fig. 4h) further verify that the O in HCHO mainly comes from O<sub>2</sub>. And the detection of HCH<sup>18</sup>O using H<sub>2</sub><sup>16</sup>O + <sup>16</sup>O<sub>2</sub> as the feed gas over Ag<sub>1</sub>-ZnO with <sup>18</sup>O exchange (Fig. 4h) also confirms the involvement of lattice oxygen in the generation of HCHO. Moreover, by comparing the effects of different O<sub>2</sub> treatments on catalysts after the photothermal catalytic oxidation of CH<sub>4</sub> under anaerobic conditions (Supplementary Fig. 32), the significance of lattice oxygen in the production of HCHO is confirmed, demonstrating that the photoactivation of O<sub>2</sub> to replenish lattice oxygen is crucial for the reaction. Based on the above results, the photothermal catalytic oxidation of CH<sub>4</sub> over Ag<sub>1</sub>-ZnO occurs via a Mars–van Krevelen mechanism. The lattice oxygen on

ZnO participates in the reaction, and the consumed oxygen sites are filled with oxygen to continue the reaction.

Based on the analysis above, the activation process of lattice oxygen plays an important role in the gas–solid photothermal catalytic selective oxidation of CH<sub>4</sub> to HCHO, so the activation effect of heat and Ag SAs on lattice oxygen in ZnO was further investigated. In the dark, the ESR signal of oxygen vacancies disappears after ZnO loading with Ag SAs in Ar, while the ESR peak signal of oxygen vacancies increases after loading Ag NPs in Ar (Fig. 4i). Under light, the peak of oxygen vacancies in Ag<sub>1</sub>-ZnO appears clearly, while the signals of ZnO and Ag<sub>NP</sub>-ZnO samples show almost no change compared to those in the dark, indicating that the loading of Ag SAs is beneficial for accelerating hole enrichment and thus facilitate the activation of surrounding lattice oxygen. At the same time, the increase in temperature also promotes the activation of lattice oxygen (Fig. 4j). The O<sub>2</sub>-TPD results (Supplementary Fig. 33) show that the peak at 153 °C attributed to the physisorption oxygen (100–200 °C) is observed in all samples, and the peak at 350–450 °C in all samples is attributed to the superficial lattice oxygen (350–600 °C)<sup>50</sup>. However, no obvious peak attributed to chemically adsorbed oxygen (200–350 °C) is observed in all samples. Moreover, for the Ag<sub>1</sub>-ZnO sample, the superficial lattice oxygen peak shifts to a lower temperature than that of the other samples, which proves that the loading Ag SAs on ZnO contributes to the mobility of lattice oxygen (the capacity of lattice oxygen converting to the surface reactive oxygen species). The desorption peak of surface lattice oxygen on Ag<sub>NP</sub>-ZnO locates at relatively higher temperature, which is due to the strong adsorption ability of Ag NPs towards oxygen species<sup>51,52</sup>. Then, crystal orbital Hamilton population (COHP) are used to analyze the covalent Zn–OCH<sub>2</sub> interactions over ZnO and Ag<sub>1</sub>-ZnO. The positive and negative values in the COHP diagram correspond to bonding and antibonding contributions, respectively<sup>53</sup>. Compared with the ZnO slab, the integrated COHP (ICOHP) value of the Ag<sub>1</sub>-ZnO slab decreases

and the Zn–O bond length increases, demonstrating that Ag SAs decrease the Zn–OCH<sub>2</sub> bonding state occupancy (Fig. 4k and Supplementary Fig. 34). Therefore, the heat and the introduction of Ag SAs can promote the activation of lattice oxygen, thereby leading to the formation of HCHO.

To obtain a full image of the possible reaction pathways for the selective oxidation of CH<sub>4</sub> to HCHO over Ag<sub>1</sub>-ZnO, DFT calculations were performed. ZnO (101) with an Ag atom (Supplementary Fig. 7c) is used for modeling, and the Gibbs free energy is corrected based on the experimental test temperature. \*OH is a key species for the activation of the C–H bond in CH<sub>4</sub> according to the isotope labeling experiment. For CH<sub>4</sub> oxidation on the Ag<sub>1</sub>-ZnO system, as shown in Fig. 4a, H<sub>2</sub>O is absorbed (reaction energy ( $\Delta E$ ) = −0.47 eV) and activated to form \*OH ( $\Delta E$  = 0.04 eV), and then the generated \*OH interrupts the C–H bond in CH<sub>4</sub> to form \*(O)CH<sub>3</sub> species and gas H<sub>2</sub>O ( $\Delta E$  = −1.17 eV). The calculation results of dissociation C–H in CH<sub>4</sub> over Ag<sub>1</sub>-ZnO indicate that \*OH prefers to break C–H in CH<sub>4</sub> than that ZnO itself (Supplementary Fig. 35). After that, the \*(O)CH<sub>3</sub> can either couple with the adsorbed \*H to form \*CH<sub>3</sub>OH or directly continue dehydrogenation to form HCHO. The  $\Delta E$  of direct \*(O)CH<sub>3</sub> dehydrogenation is −1.83 eV, and the competing pathway of \*CH<sub>3</sub>OH formation must overcome a barrier ( $E_a$ ) of 0.61 eV. The \*CH<sub>3</sub>OH desorption to form CH<sub>3</sub>OH still requires a  $\Delta E$  of 0.73 eV. That is, \*(O)CH<sub>3</sub> is more inclined to continue dehydrogenation. Then, the dissociated \*(O)CH<sub>2</sub> group was attached on the Ag atom with O–Ag bridge to form \*HCHO ( $E_a$  = 0.20 eV,  $\Delta E$  = −0.54 eV). \*HCHO undergoes desorption to generate HCHO ( $\Delta E$  = 0.60 eV). Finally, O<sub>2</sub> is activated and replenishes the consumed lattice oxygen. After comparing with the simulation results of the HCHO formation process on pure ZnO (Supplementary Fig. 37), it can be concluded that Ag SAs doping facilitates the desorption of HCHO and the replenishment of lattice oxygen, which agrees with the above characterization results. In addition, the Gibbs free energy results at different temperatures also indicate that an increase in reaction temperature can effectively promote the generation of HCHO (Fig. 5a, Supplementary Figs. 36 and 37).

A reaction mechanism for the gas–solid photothermal catalytic selective oxidation of CH<sub>4</sub> to HCHO on Ag<sub>1</sub>-ZnO is proposed in Fig. 5b, c. Under thermal action, photogenerated electrons and holes on ZnO rapidly separate to form Zn<sup>+</sup>O<sup>−</sup> active sites under irradiation. The holes on O<sup>−</sup> transfer to Ag SAs and then extract the H atom from CH<sub>4</sub> to form \*CH<sub>2</sub> species under the action of the surface \*OH species. Then, the activation of lattice oxygen is promoted under the joint action of heat and Ag SAs, thereby facilitating the formation and desorption of \*HCHO to form HCHO. Finally, the electrons on Zn<sup>+</sup> activate O<sub>2</sub> to form O<sub>2</sub><sup>−</sup>, replenishing the consumed lattice oxygen.

## Discussion

To summarize, we propose a continuous-flow gas–solid photothermal catalysis strategy under ambient pressure to overcome application bottlenecks regarding products concentration of traditional gas–liquid–solid photocatalysis. The rationally designed Ag<sub>1</sub>-ZnO photocatalyst has been proven to be a suitable photocatalyst. The Ag SAs accumulate photogenerated holes, which promote the C–H bond cleavage of CH<sub>4</sub> with the assistance of \*OH. And Ag SAs alter the local electron distribution of ZnO, which is beneficial for the formation and desorption of \*HCHO to generate gas-phase HCHO. Furthermore, the heat input promotes the separation of photogenerated electrons and holes, and enhances the mobility of surface lattice oxygen, thus promoting the formation of HCHO. An ultrahigh HCHO (514.2 ± 33.7 μmol mL<sup>−1</sup>; 1.54 ± 0.10 wt.%) concentration is obtained with water absorption of the gases after a 12-hour reaction. With rational catalyst design, optimization of catalytic systems, and understanding of the

mechanism, this work has laid a solid foundation for the sustainable selective oxidation of CH<sub>4</sub> into valuable chemicals in industry.

## Methods

### Materials

All chemicals were used without further purification. Oxalic acid dihydrate (H<sub>2</sub>C<sub>2</sub>O<sub>4</sub>·2H<sub>2</sub>O, 99.99%), zinc nitrate hexahydrate (Zn(NO<sub>3</sub>)<sub>2</sub>·6H<sub>2</sub>O) and ethanol (CH<sub>3</sub>CH<sub>2</sub>OH, 99.5%) were bought from Sinopharm Chemical Reagent Co., Ltd. (Shanghai, China). Hydrogen tetrachloroaurate(III) trihydrate (HAuCl<sub>4</sub>·3H<sub>2</sub>O, ≥99.9%), silver nitrate (AgNO<sub>3</sub>, ≥99.98%), hexahydrate chloroplatinic acid (H<sub>2</sub>PtCl<sub>6</sub>·6H<sub>2</sub>O, ≥99.9%) and palladium chloride (PdCl<sub>2</sub>, ≥99.9%) were purchased from Aladdin Chemical Co. Ltd. (Shanghai, China). Deuterium water (D<sub>2</sub>O, 98%) and heavy oxygen water (H<sub>2</sub><sup>18</sup>O, 98%) were purchased from Shanghai Yuanye Bio-Technology Co., Ltd (Shanghai, China). Dimethyl sulfoxide (DMSO, 99.99%) was purchased from Beijing Vokai Bio-technology Co., LTD (Beijing, China). Methane (CH<sub>4</sub>, 99.999%), air (99.9995%), Argon (Ar, ≥99.999%) and Oxygen-18 (<sup>18</sup>O<sub>2</sub>, 99%) were purchased from Dalian Special Gas Co., Ltd. (Dalian, China).

### Synthesis of ZnO NPs

ZnO NPs were synthesized as following. First, a solution of H<sub>2</sub>C<sub>2</sub>O<sub>4</sub> (50 mM, 100 mL) was added dropwise to a stirred solution of Zn(NO<sub>3</sub>)<sub>2</sub> solution (50 mM, 100 mL) to obtain a zinc oxalate precipitate. Then the precipitate was washed with deionized water several times and dried overnight at 80 °C. The obtained zinc oxalate powder (5.00 g) was calcined in a muffle furnace at 350 °C for 6 h with a heating rate of 5 °C min<sup>−1</sup> to obtain ZnO NPs.

### Synthesis of Ag<sub>1</sub>-ZnO and Ag<sub>NP</sub>-ZnO

Ag<sub>1</sub>-ZnO and Ag<sub>NP</sub>-ZnO were synthesized through a simple sodium hypophosphite (NaH<sub>2</sub>PO<sub>2</sub>) reduction method. Specifically, ZnO NPs (50.0 mg) were dispersed in deionized water (50 mL) by sonication (30 min), followed by adding 158.0 μL (Ag<sub>1</sub>-ZnO, 0.912 μmol Ag) or 789.9 μL (Ag<sub>NP</sub>-ZnO, 4.56 μmol Ag) of AgNO<sub>3</sub> solution (5.76 mM) and stirring for 1 h. Then, sodium hypophosphite (5.78 mM) with a molar weight of 5 times AgNO<sub>3</sub> was added dropwise to the above solution at 85 °C and stirred for 1.5 h. The obtained photocatalysts were washed several times with deionized water and dried under vacuum at 80 °C overnight. For comparison experiments, Au<sub>1</sub>-ZnO, Pt<sub>1</sub>-ZnO and Pd<sub>1</sub>-ZnO containing the same metal mass were successfully synthesized using the above method in addition to using HAuCl<sub>4</sub>, H<sub>2</sub>PtCl<sub>6</sub> and PdCl<sub>2</sub> as the corresponding metal precursors.

### Synthesis of Ag<sub>1</sub>-ZnO with <sup>18</sup>O exchange

For the isotope labeling experiment, 0.1 g of Ag<sub>1</sub>-ZnO was treated under a flow of Ar gas (100 mL min<sup>−1</sup>) bubbling through H<sub>2</sub><sup>18</sup>O at 350 °C for 2 h to exchange the lattice <sup>16</sup>O with <sup>18</sup>O. This was followed by another 2 h of Ar treatment without H<sub>2</sub><sup>18</sup>O at 350 °C to remove the residual H<sub>2</sub><sup>18</sup>O or <sup>−18</sup>OH on the surface.

### Photothermal catalytic activity measurements

Photothermal catalytic oxidation of CH<sub>4</sub> was conducted in a 50-mL flow reactor (PLR-GPTR50, Beijing Perfectlight) at different temperatures under a 300-W Xenon lamp (PLS-SXE300+, Beijing Perfectlight). The light was at a wavelength of 200 nm < λ < 1200 nm and the light intensity was 1000 mW/cm<sup>2</sup>. The schematic diagram of the experimental device and the physical photo of the reaction device are shown in Supplementary Fig. 8. In a typical test, 1.0 mL of an aqueous photocatalyst dispersion (4 mg mL<sup>−1</sup>) after 30 min of ultrasound was uniformly dropped into a quartz vessel (diameter 4 cm, height 1 cm), and then the obtain quartz vessel was dried at 353 K and placed in the reactor. Then the reactor was heated to a certain temperature, and different highly pure CH<sub>4</sub> (99.999%)/air (99.999%, O<sub>2</sub>/N<sub>2</sub> = 25 vol%) values at a total flow rate of 50 mL min<sup>−1</sup> and different RH values



(controlling the amount of wet air prepared by bubbling the air through 25 °C water) passed through the reactor to replace the gas for 30 min. After that, the light was turned on for the reaction. The temperature of the catalyst surface was measured using a thermocouple at the bottom of the quartz vessel as shown in Supplementary Fig. 8b.

CO, CO<sub>2</sub>, C<sub>2</sub>H<sub>6</sub> and CH<sub>3</sub>OH content were based on the calibration curve by detected via gas chromatography (GC, FULIGC9790II) equipped with a methanizer and a flame ionization detector using a column (Porapak Q) (Supplementary Fig. 9). The gaseous HCHO was collected by introducing it into 50 mL of water for 5 min at 0 °C, and the amount of HCHO in the absorption solution was determined by the colorimetric method (Hitachi U4100). The concentrations of HCHO and CH<sub>3</sub>OH in the 3 h and 12 h absorption solutions were quantified by colorimetric method and <sup>1</sup>H NMR (WNMR-I400), respectively. For detecting HCHO, 5 mL of the absorption solution was mixed with as-prepared 1 mL 0.25% (v/v) acetylacetone solution and the mixed solution was kept in boiling water for 3 min. The HCHO content was based on the calibration curve by detecting the absorption intensity at 413 nm (Supplementary Fig. 10). For detecting CH<sub>3</sub>OH, 0.5 mL absorption solution was mixed with 0.1 mL D<sub>2</sub>O and 0.05 μL DMSO. The concentration of CH<sub>3</sub>OH was calculated based on the internal standard DMSO.

The selectivity of HCHO was defined as follows: HCHO selectivity = the number of moles of HCHO/the number of moles of (CO + CO<sub>2</sub> + C<sub>2</sub>H<sub>6</sub> + CH<sub>3</sub>OH + HCHO) × 100%. The selectivity of the CO + CH<sub>3</sub>OH + HCHO products was calculated as follows: CO + CH<sub>3</sub>OH + HCHO selectivity = the number of moles of (CO + CH<sub>3</sub>OH + HCHO)/the number of moles of (CO + CO<sub>2</sub> + C<sub>2</sub>H<sub>6</sub> + CH<sub>3</sub>OH + HCHO) × 100%.

AQY of HCHO over Ag<sub>1</sub>-ZnO was determined using the following equation:

$$\text{AQY(HCHO)} = \frac{N(\text{electrons})}{N(\text{photons})} \times 100\% \quad (1)$$

where  $N(\text{electrons})$  and  $N(\text{photons})$  represent the number of reacted electrons and the number of incident photons, respectively. In accordance with the chemical equation ( $\text{CH}_4 - 4\text{e}^- \rightarrow \text{HCHO}$ )<sup>10,11,54</sup>,  $N(\text{electrons}) = 4 \times N(\text{HCHO}) = 4 \times M(\text{HCHO})N_A$ , where  $N(\text{HCHO})$ ,  $M(\text{HCHO})$  and  $N_A$  represent the number of produced HCHO molecules, the number of HCHO moles and Avogadro's constant, respectively. The number of incident photons is calculated as  $N(\text{photons}) = IAt/E_\lambda$ , where  $I$ ,  $A$ ,  $t$  and  $E_\lambda$  denote light intensity ( $\text{W cm}^{-2}$ ), irradiation area ( $\text{cm}^2$ ), light incident time (s) and photon energy (J), respectively.  $E_\lambda = hc/\lambda$  ( $\lambda = 365, 400$  or  $420$  nm). The light intensity  $I$  at different wavelengths (365, 400 and 420 nm) was 0.00764, 0.0879, and 0.110  $\text{W cm}^{-2}$ , and the irradiation area coated with 20 mg catalyst was  $A = 12.56 \text{ cm}^2$ . The surface temperature of the catalyst was controlled approximately 228 °C under monochromatic light irradiation.

## Characterizations

Powder XRD (BRUKER D8 Advance) was carried out with Cu K $\alpha$  radiation to obtain the crystalline structure of the photocatalysts. TEM (JEOL JEM-F200) and STEM (JEOL JSM-7500F) were performed to observe the morphology of the photocatalysts. The contents of precious metals (Au, Ag, Pt, and Pd) in the samples were measured by ICP-OES (Agilent 720). XPS (Escalab 250Xi) was used to detect the surface chemistry of photocatalysts. In situ NAP-XPS measurements were carried out on a SPECS NAP-XPS system. The Ag K-edge X-ray absorption near-edge structure (XANES) and extended X-ray absorption fine structure (EXAFS) of the samples were collected under ambient conditions, where a pair of channel-cut Si (111) crystals was used in the monochromator. The Ag<sub>1</sub>-ZnO data were obtained in the fluorescence mode. The reference Ag foil and Ag<sub>NP</sub>-ZnO were

measured in transmission mode. The energy of the storage ring was 2.5 GeV with an average electron current of <200 mA.

The optical properties of the photocatalysts were determined by UV-vis diffuse reflectance spectroscopy (Hitachi U4100). The PL (FLS 980), transient photocurrent (TPC), and electrochemical impedance (EIS) of the photocatalyst were obtained to evaluate its photoelectric activity. The TPC and EIS were performed in a 0.1 M Na<sub>2</sub>SO<sub>4</sub> aqueous. A fluorine-doped tin oxide electrode coated with the photocatalyst, a platinum wire, and saturated calomel electrodes were tested under a 300-W xenon lamp as the working, counter, and reference electrodes, respectively. The working electrodes were prepared using the colloid drop coating method. 5 mg of photocatalyst was dispersed in a mixed solution (0.01 mL of 5% Nafion, 0.2 mL of isopropanol and 0.6 mL of water) with ultrasonication.

In situ ESR spectra were measured on a JES-FA 200 JOES spectrometer. In the test, the sample (20 mg) was placed in a nuclear magnetic resonance tube under different atmospheres for 20 min. The ESR data were then recorded under full-spectrum illumination at different temperatures. Due to the influence of temperature on the peak signal, the highest test temperature in this study was 75 °C.

In situ DRIFTS test for photocatalytic selective oxidation of CH<sub>4</sub> was conducted on a Nicolet 6700 FTIR spectrometer. First, the samples were pretreated at 350 °C for 1 h using N<sub>2</sub> with a flow rate of 50 mL min<sup>-1</sup> to remove the residual substances on the photocatalyst surface. Then the CH<sub>4</sub> mixed gas (CH<sub>4</sub>: Air = 45: 5, RH = 20%, flow rate = 50 mL min<sup>-1</sup>) was passed through the reaction chamber at different temperatures for 30 min to reach the gas-solid stable state. The background spectrum with the CH<sub>4</sub> mixed gas flow was recorded at the different temperatures and was then subtracted from the total spectra. The samples were scanned 30 times (each time per 60 s) under 300-W xenon lamp irradiation.

In situ DRIFTS of CO adsorption was conducted on a Bruker Tensor 27 FTIR spectrometer. First, all photocatalysts were treated with pure He at a flow rate of 30 mL min<sup>-1</sup> and a temperature of 150 °C for 1 h before cooling. After the samples were cooled to 30 °C, the background spectrum was recorded at a flow of 30 mL min<sup>-1</sup> He, and CO/He (2 vol.%) was then introduced into the reaction cell at a flow of 30 mL min<sup>-1</sup>. Then, pure He was passed again through the reaction chamber at a flow of 30 mL min<sup>-1</sup> to desorb the gaseous CO. Spectra were recorded during all the processes.

O<sub>2</sub>-TPO, O<sub>2</sub>-TPD and HCHO-TPD were conducted on a custom-made multipurpose adsorption instrument (DAS-7000, Guangzhou Huasi Co., Ltd., China). For O<sub>2</sub>-TPO, 50 mL min<sup>-1</sup> O<sub>2</sub> was introduced to the sample (0.1 g) at 30 °C, after which the temperature was increased from 30 to 800 °C at a rate of 10 °C min<sup>-1</sup>, and the data were recorded. For O<sub>2</sub>-TPD, the sample (0.1 g) was pretreated with pure He (flow rate = 50 mL min<sup>-1</sup>) at 150 °C for 1 h, the temperature was then reduced to 30 °C, and the sample was treated with a flow of O<sub>2</sub> for 2 h. Then, the O<sub>2</sub> flow was switched to a flow of He, after which the temperature was increased from 50 to 800 °C at a rate of 10 °C min<sup>-1</sup>, and the data were recorded. The method of HCHO-TPD is consistent with the testing method of O<sub>2</sub>-TPD, except for changing O<sub>2</sub> adsorption to 50 ppm HCHO standard gas adsorption after He gas treatment at 350 °C.

## Computational methods

The Vienna ab initio Simulation Package (VASP5.4.4) was used to perform all spin-polarized DFT simulations within the generalized gradient approximation (GGA) based on a Perdew-Burke-Ernzerhof (PBE)<sup>55,56</sup>. A generalized gradient approximation was chosen. The core-valence electron interactions were described using the projector augmented-wave method. The first Brillouin zone was sampled with a 3 × 1 × 1 Monkhorst-Pack grid<sup>57</sup>. The plane wave energy cutoff was set to 400 eV to optimize the geometric structures. The energy and electronic force convergence tolerances were below 1 × 10<sup>-5</sup> eV and 0.02 eV/Å, respectively. The reaction pathway was explored with the

NEB method, with Climbing image or Dimer method to locate the transition state. Based on the comparison between the calculated coordination and bond length of Ag single atoms on different facets (Supplementary Fig. 7c) and the EXAFS fitting results of Ag<sub>1</sub>-ZnO (Supplementary Table 1), ZnO (101) was used for DFT calculations. The optimized ZnO (101) supercell ( $p \times 2 \times 5$ ) parameters were  $a = 12.27 \text{ \AA}$ ,  $b = 16.25 \text{ \AA}$ ,  $c = 20 \text{ \AA}$ ,  $\alpha = \beta = 90^\circ$ , and  $\gamma = 105^\circ$ . The free energy of the reaction on the surface was calculated as  $G(T) = \varepsilon_{\text{ele}} + \Delta ZPE + \Delta H - T\Delta S$ , where  $\varepsilon_{\text{ele}}$ ,  $\Delta ZPE$ ,  $T$ ,  $\Delta H$  and  $\Delta S$  were the total energy for the adsorption of intermediates on the model surface, the zero-point energy change, the reaction temperature, the enthalpy change, and the entropy change, respectively.

## Data availability

All relevant data generated in this study are provided in the Supplementary Information/Source Data file. Atomic coordinates of the optimized structure are provided in Supplementary Data. The data that support this study are available from the corresponding author upon reasonable request. Source data are provided with this paper.

## References

- Heim, L. E., Konnerth, H. & Pechtl, M. H. G. Future perspectives for formaldehyde: pathways for reductive synthesis and energy storage. *Green. Chem.* **19**, 2347–2355 (2017).
- Trincado, M., Grützmaier, H. & Pechtl, M. H. G. CO<sub>2</sub>-based hydrogen storage – Hydrogen generation from formaldehyde/water. *Phys. Sci. Rev.* **3**, 20170013 (2018).
- Li, R. et al. Oxygen-Controlled Hydrogen Evolution Reaction: Molecular Oxygen Promotes Hydrogen Production from Formaldehyde Solution Using Ag/MgO Nanocatalyst. *ACS Catal.* **7**, 1478–1484 (2017).
- Bahmanpour, A. M., Hoadley, A. & Tanksale, A. Formaldehyde production via hydrogenation of carbon monoxide in the aqueous phase. *Green. Chem.* **17**, 3500–3507 (2015).
- Sam, B., Breit, B. & Krische, M. J. Paraformaldehyde and Methanol as C1 Feedstocks in Metal-Catalyzed C-C Couplings of  $\pi$ -Unsaturated Reactants: Beyond Hydroformylation. *Angew. Chem. Int. Ed.* **54**, 3267–3274 (2015).
- Jiang, Y., Li, S., Fan, X. & Tang, Z. Recent advances on aerobic photocatalytic methane conversion under mild conditions. *Nano Res.* **16**, 12558–12571 (2023).
- Li, X., Wang, C. & Tang, J. Methane transformation by photocatalysis. *Nat. Rev. Mater.* **7**, 617–632 (2022).
- Li, Q., Ouyang, Y., Li, H., Wang, L. & Zeng, J. Photocatalytic conversion of methane: Recent advancements and prospects. *Angew. Chem. Int. Ed.* **61**, e202108069 (2022).
- Song, H. & Ye, J. Direct Photocatalytic Conversion of Methane to Value-Added Chemicals. *Trends Chem.* **4**, 1094–1105 (2022).
- Jiang, Y. et al. Steering Photooxidation of Methane to Formic Acid over A Priori Screened Supported Catalysts. *J. Am. Chem. Soc.* **146**, 16039–16051 (2024).
- Jiang, Y. et al. Elevating photooxidation of methane to formaldehyde via TiO<sub>2</sub> crystal phase engineering. *J. Am. Chem. Soc.* **144**, 15977–15987 (2022).
- Luo, L. et al. Nearly 100% selective and visible-light-driven methane conversion to formaldehyde via single-atom Cu and W<sup>5+</sup>. *Nat. Commun.* **14**, 2690 (2023).
- Fan, Y. et al. Selective photocatalytic oxidation of methane by quantum-sized bismuth vanadate. *Nat. Sustain.* **4**, 509–515 (2021).
- Song, H. et al. Direct and selective photocatalytic oxidation of CH<sub>4</sub> to oxygenates with O<sub>2</sub> on cocatalysts/ZnO at room temperature in water. *J. Am. Chem. Soc.* **141**, 20507–20515 (2019).
- Wei, S. et al. Aerobic oxidation of methane to formaldehyde mediated by crystal-O over gold modified tungsten trioxide via photocatalysis. *Appl. Catal. B Environ.* **283**, 119661 (2021).
- An, B. et al. Direct Photo-oxidation of Methane to Methanol over A Mono-iron Hydroxyl Site. *Nat. Mater.* **21**, 932–938 (2022).
- Cao, Y. et al. Methane photooxidation with nearly 100% selectivity towards oxygenates: Proton rebound ensures the regeneration of methanol. *Angew. Chem. Int. Ed.* **62**, e202302196 (2023).
- Han, C. et al. Selective cleavage of chemical bonds in targeted intermediates for highly selective photooxidation of methane to methanol. *J. Am. Chem. Soc.* **145**, 8609–8620 (2023).
- Wang, A., Li, J. & Zhang, T. Heterogeneous single-atom catalysis. *Nat. Rev. Chem.* **2**, 65–81 (2018).
- Liang, X., Fu, N., Yao, S., Li, Z. & Li, Y. The progress and outlook of metal single-atom-site catalysis. *J. Am. Chem. Soc.* **144**, 18155–18174 (2022).
- Zhang, Y. et al. Simultaneous generation of ammonia during nitrile waste gas purification over a silver single-atom-doped ceria catalyst. *Environ. Sci. Technol.* **57**, 12513–12522 (2023).
- Jiang, Y. et al. Enabling specific photocatalytic methane oxidation by controlling free radical type. *J. Am. Chem. Soc.* **145**, 2698–2707 (2023).
- Sun, Z., Wang, C. & Hu, Y. H. Highly selective photocatalytic conversion of methane to liquid oxygenates over silicomolybdenic acid/TiO<sub>2</sub> under mild conditions. *J. Mater. Chem. A* **9**, 1713–1719 (2021).
- Chen, X. et al. Photocatalytic oxidation of methane over silver decorated zinc oxide nanocatalysts. *Nat. Commun.* **7**, 12273 (2016).
- Hu, D., Addad, A., Ben Tayeb, K., Ordonsky, V. V. & Khodakov, A. Y. Thermocatalysis enables photocatalytic oxidation of methane to formic acid at room temperature beyond the selectivity limits. *Cell Rep. Phys. Sci.* **4**, 101277 (2023).
- Zhang, R. et al. Direct Photocatalytic Methane Oxidation to Formaldehyde by N Doping Co-Decorated Mixed Crystal TiO<sub>2</sub>. *ACS Nano* **18**, 12994–13005 (2024).
- Mahlaba, S. V. L., Hyttoolakhanlal Mahomed, N., Leteba, G. M., Govender, A. & van Steen, E. Role of Support in the Selective, Aerobic Methane Oxidation to Formaldehyde over Pt/TiO<sub>2</sub>. *ACS Catal.* **13**, 14770–14781 (2023).
- Mahlaba, S. V. L. et al. Platinum-Catalysed Selective Aerobic Oxidation of Methane to Formaldehyde in the Presence of Liquid Water. *Angew. Chem. Int. Ed.* **61**, e202206841 (2022).
- Yang, Y. et al. Bioinspired Cu(II) Defect Sites in ZIF-8 for Selective Methane Oxidation. *J. Am. Chem. Soc.* **145**, 22019–22030 (2023).
- Taiki, A., Mana, S. & Sakae, T. Superior Performance of Copper Phosphate  $\alpha$ -Cu<sub>2</sub>P<sub>2</sub>O<sub>7</sub> Catalysts for Partial Oxidation of Methane into Formaldehyde. *Chem. Lett.* **51**, 511–514 (2022).
- Tian, J. et al. Direct conversion of methane to formaldehyde and CO on B<sub>2</sub>O<sub>3</sub> catalysts. *Nat. Commun.* **11**, 5693 (2020).
- Otsuka, K. & Hatano, M. The catalysts for the synthesis of formaldehyde by partial oxidation of methane. *J. Catal.* **108**, 252–255 (1987).
- Li, Y., An, D., Zhang, Q. & Wang, Y. Copper-Catalyzed Selective Oxidation of Methane by Oxygen: Studies on Catalytic Behavior and Functioning Mechanism of CuOx/SBA-15. *J. Phys. Chem. C* **112**, 13700–13708 (2008).
- Wang, Y. et al. SBA-15-supported iron phosphate catalyst for partial oxidation of methane to formaldehyde. *Catal. Today* **93–95**, 155–161 (2004).
- Berndt, H. et al. Structure and Catalytic Properties of VO<sub>x</sub>/MCM Materials for the Partial Oxidation of Methane to Formaldehyde. *J. Catal.* **191**, 384–400 (2000).
- Volodin, A. M. & Cherkashin, A. E. ERS spectrum of methyl radicals on ZnO surface. *React. Kinet. Catal. Lett.* **18**, 243–246 (1982).
- Kaftelen, H. et al. EPR and photoluminescence spectroscopy studies on the defect structure of ZnO nanocrystals. *Phys. Rev. B* **86**, 014113 (2012).

38. Gaarenstroom, S. W. & Winograd, N. Initial and final state effects in the ESCA spectra of cadmium and silver oxides. *J. Chem. Phys.* **67**, 3500–3506 (1977).
39. Kaushik, V. K. XPS core level spectra and Auger parameters for some silver compounds. *J. Electron Spectrosc. Relat. Phenom.* **56**, 273–277 (1991).
40. Zhang, W. et al. High-performance photocatalytic nonoxidative conversion of methane to ethane and hydrogen by heteroatoms-engineered TiO<sub>2</sub>. *Nat. Commun.* **13**, 2806 (2022).
41. Jiang, W. et al. Pd-modified ZnO-Au enabling alkoxy intermediates formation and dehydrogenation for photocatalytic conversion of methane to ethylene. *J. Am. Chem. Soc.* **143**, 269–278 (2021).
42. Pak, S., Qiu, P. & Lunsford, J. H. Elementary reactions in the oxidative coupling of methane over Mn/Na<sub>2</sub>WO<sub>4</sub>/SiO<sub>2</sub> and Mn/Na<sub>2</sub>WO<sub>4</sub>/MgO catalysts. *J. Catal.* **179**, 222–230 (1998).
43. Kähler, K., Holz, M. C., Rohe, M., Strunk, J. & Muhler, M. Probing the reactivity of ZnO and Au/ZnO nanoparticles by methanol adsorption: a TPD and DRIFTS study. *Chemphyschem* **11**, 2521–2529 (2010).
44. Wang, Y. et al. Photocatalytic Oxidative Coupling of Methane over Au<sub>1</sub>Ag Single-Atom Alloy Modified ZnO with Oxygen and Water Vapor: Synergy of Gold and Silver. *Angew. Chem. Int. Ed.* **62**, e202310525 (2023).
45. Cao, Y. et al. Probing surface defects of ZnO using formaldehyde. *J. Chem. Phys.* **152**, 074714 (2020).
46. Yan, B. et al. A Comparison of various FTIR and FT Raman methods: Applications in the reaction optimization stage of combinatorial chemistry. *J. Combinatorial Chem.* **1**, 46–54 (1999).
47. Li, Q. et al. Oxygen vacancies mediated flower-like BiOX microspheres for photocatalytic purification of methyl mercaptan odor: Significant distinction induced by halogen elements. *Chem. Eng. J.* **471**, 144658 (2023).
48. Wang, Y., Zhang, Y., Liu, Y. & Wu, Z. Photocatalytic oxidative coupling of methane to ethane using water and oxygen on Ag<sub>3</sub>PO<sub>4</sub>-ZnO. *Environ. Sci. Technol.* **57**, 11531–11540 (2023).
49. Song, S. et al. A selective Au-ZnO/TiO<sub>2</sub> hybrid photocatalyst for oxidative coupling of methane to ethane with dioxygen. *Nat. Catal.* **4**, 1032–1042 (2021).
50. Weng, X. et al. Catalytic oxidation of chlorinated organics over lanthanide perovskites: effects of phosphoric acid etching and water vapor on chlorine desorption behavior. *Environ. Sci. Technol.* **53**, 884–893 (2019).
51. Gao, Y. et al. Study of Ag/Ce<sub>x</sub>Nd<sub>1-x</sub>O<sub>2</sub> nanocubes as soot oxidation catalysts for gasoline particulate filters: Balancing catalyst activity and stability by Nd doping. *Appl. Catal. B Environ.* **203**, 116–126 (2017).
52. Liu, S. et al. Soot oxidation over CeO<sub>2</sub> and Ag/CeO<sub>2</sub>: Factors determining the catalyst activity and stability during reaction. *J. Catal.* **337**, 188–198 (2016).
53. Steinberg, S. & Dronskowski, R. The Crystal Orbital Hamilton Population (COHP) Method as a Tool to Visualize and Analyze Chemical Bonding in Intermetallic Compounds. *Crystals* **8**, 225 (2018).
54. Fan, Y. et al. Insight into selectivity of photocatalytic methane oxidation to formaldehyde on tungsten trioxide. *Nat. Commun.* **15**, 4679 (2024).
55. Kresse, G. & Joubert, D. From ultrasoft pseudopotentials to the projector augmented-wave method. *Phys. Rev. B* **59**, 1758–1775 (1999).
56. Perdew, J. P., Burke, K. & Ernzerhof, M. Generalized Gradient Approximation Made Simple. *Phys. Rev. Lett.* **77**, 3865–3868 (1996).
57. Blochl, P. E. Projector augmented-wave method. *Phys. B Condens. Matter* **50**, 17953–17979 (1994).

## Acknowledgements

We gratefully acknowledge the financial support from the National Natural Science Foundation of China (No. 22276162 (Y.L.), 51878598 (Z.W.)).

## Author contributions

Y.W., Y.L., and Z.W. conceived the idea for this work. Y.W. and Y.Z. prepared the photocatalysts, and performed the characterizations and catalytic measurements. Y.W., X.W., and Y.L. analyzed and processed the data. Y.W. and Y.Z. carried out the DFT calculations. Y.W., Y.L., and Y.Z. wrote the manuscript. All the authors contributed to the interpretation of the data and the preparation of the manuscript.

## Competing interests

The authors declare no competing interests.

## Additional information

**Supplementary information** The online version contains supplementary material available at <https://doi.org/10.1038/s41467-025-57854-y>.

**Correspondence** and requests for materials should be addressed to Yue Liu or Zhongbiao Wu.

**Peer review information** *Nature Communications* thanks Zheng Xiao Guo and the other, anonymous, reviewers for their contribution to the peer review of this work. A peer review file is available.

**Reprints and permissions information** is available at <http://www.nature.com/reprints>

**Publisher's note** Springer Nature remains neutral with regard to jurisdictional claims in published maps and institutional affiliations.

**Open Access** This article is licensed under a Creative Commons Attribution-NonCommercial-NoDerivatives 4.0 International License, which permits any non-commercial use, sharing, distribution and reproduction in any medium or format, as long as you give appropriate credit to the original author(s) and the source, provide a link to the Creative Commons licence, and indicate if you modified the licensed material. You do not have permission under this licence to share adapted material derived from this article or parts of it. The images or other third party material in this article are included in the article's Creative Commons licence, unless indicated otherwise in a credit line to the material. If material is not included in the article's Creative Commons licence and your intended use is not permitted by statutory regulation or exceeds the permitted use, you will need to obtain permission directly from the copyright holder. To view a copy of this licence, visit <http://creativecommons.org/licenses/by-nc-nd/4.0/>.

© The Author(s) 2025